Energy & Environmental Science

ROYAL SOCIETY OF CHEMISTRY

PAPER

View Article Online
View Journal | View Issue

Cite this: *Energy Environ. Sci.*, 2023, **16**, 663

Energy-efficient electrochemical ammonia production from dilute nitrate solution†

Keon-Han Kim,[a] Heebin Lee,[b] Xiaopeng Huang,[ac] Jong Hui Choi,[b] Chunping Chen,[a] Jeung Ku Kang *[b] and Dermot O'Hare *[a]

Received 25th October 2022,
Accepted 9th January 2023

DOI: 10.1039/d2ee03461a

rsc.li/ees

Highly efficient electrochemical nitrate reduction could become a key process for sustainable ammonia production overcoming many limitations of the Haber–Bosch process. Current state-of-the-art electrocatalysts have severe drawbacks regarding yield, selectivity and energy efficiency when dealing with dilute nitrate solutions. Herein, we report a layered double hydroxide (LDH)/Cu foam hybrid electrocatalyst that offers a potential solution to this challenge. The $[Ni_{0.75}Fe_{0.25}(OH)_2](CO_3)_{0.125}$ (Ni_3Fe–CO_3 LDH) exhibits an appropriate kinetic energy barrier for the Volmer step generating hydrogen radicals as well as suppressing H–H bond formation by inhibition of the Heyrovsky step. The electrochemically generated hydrogen radicals transfer to a Cu surface enabling NO_3^- reduction to NH_3. The Ni_3Fe–CO_3 LDH/Cu foam hybrid electrode exhibits an 8.5-fold higher NH_3 yield compared to a pristine Cu surface, while exhibiting an NH_3 selectivity of 95.8% at 98.5% NO_3^- conversion. The best half-cell energy efficiency (36.6%) was recorded while achieving 96.8% faradaic efficiency at −0.2 V in 5 mM $NO_3^-{}_{(aq)}$.

Broader context

Significant attention has recently been directed towards developing electrocatalysts as an alternative technology to the traditional Haber–Bosch process. An alternative approach could involve the electrocatalytic reduction of nitrate (NO_3^-) to ammonia (NH_3). To provide a sustainable and energy-efficient technical solution will require the use of earth abundant elements as well as utilising natural sources of NO_3^- (below 10 mM). Herein, we report an energy-efficient hybrid electrocatalyst for the reduction dilute NO_3^- solution to ammonia. The electrocatalyst operates *via* a hydrogen radical strategy leading to ultrahigh performance for NH_3 production at low NO_3^- concentrations, thus paving the way to realising a sustainable and energy-efficient NH_3 economy.

1 Introduction

The high energy density of ammonia (4.32 kW h L^{-1}) means it has become an chemical of high interest as we consider carbon free energy carries in addition to remaining a pivotal feedstock of the agricultural, plastic, pharmaceutical and textile industries.[1–4] For over 100 years the Haber–Bosch process has monopolised NH_3 production; utilising 1–2% of the world's energy supply and producing 1% of the total global energy related CO_2 emissions in order to produce NH_3.[5,6] Furthermore, 80% of the energy demand derives from steam methane reforming (SMR) to supply H_2 gas as a feedstock to the Haber–Bosch process. Electrochemical H_2 production using electricity from renewable technologies and its subsequent utilization could be a source of 'green NH_3'. Although the efficiency and stability of polymer electrolyte membrane (PEM) electrolysers for green H_2 production have developed significantly, it requires at least 30.3–35.3 GJ per $ton_{ammonia}$ at an operating efficiency of even up to 60–70%. Additionally, N_2 production requires additional 2.7 GJ per $ton_{ammonia}$ using an air-separation unit and Haber–Bosch loop compressors to supply N_2 to proceed the Haber–Bosch process with green H_2. These costs are currently still higher than the conventional Haber–Bosch process (below 30 GJ per $ton_{ammonia}$).[54,55] In this regard, electrochemical nitrogen reduction (NRR) has recently sparked global research interests to produce NH_3 as an alternative to Haber–Bosch process. To date, it has suffered from low yield (below 3×10^{-10} mol s^{-1} cm^{-2}) and faradaic efficiency (FE, lower than 10%), challenged by the N≡N bond strength (941 kJ mol^{-1}), poor N_2 solubility in aqueous solution (0.66 mmol L^{-1} under ambient conditions), and the competing hydrogen evolution reaction (HER).[7,8]

[a] *Department of Chemistry, Chemical Research Laboratory, University of Oxford, OX1 3TA, UK. E-mail: dermot.ohare@chem.ox.ac.uk*
[b] *Department of Materials Science and Engineering, Korea Advanced Institute of Science and Technology (KAIST), 291 Daehak-ro, Yuseong-gu, Daejeon 34141, Republic of Korea. E-mail: jeung@kaist.ac.kr*
[c] *Department of Chemistry, Faculty of Arts and Sciences, Beijing Normal University, Zhuhai 519087, China*

† Electronic supplementary information (ESI) available. See DOI: https://doi.org/10.1039/d2ee03461a

Electrochemical nitrate reduction (NitRR) has the potential to offer a sustainable route to solve the environmental issues of denitrification and the energy demands of NH_3 production. Low N=O bonding energy (204 kJ mol^{-1}) and high NO_3^- solubility offer the potential for high electrocatalytic performance of NitRR compared to NRR.[9] In recent years, some NitRR electrocatalysts have been developed that can surpass the NH_3 yield of Haber–Bosch process (<0.2 mol $g_{catalyst}^{-1}$ h^{-1})[10,11] and exceed the current density of 2 A cm^{-2} for NH_3 production.[12] In spite of these achievements, high-yield NH_3 production from NO_3^- presents two major obstacles that need to be improved if it is to deliver a scalable practical solution. Firstly, highly performing electrocatalysts typically operate in highly concentrated NO_3^- electrolyte (100–1000 mM),[5,10,13–16] requiring additional and expensive costs associated with concentrating nitrate solutions. In reality, most nitrate sources such as textile industrial wastewater (<10 mM) and polluted ground water (<2 mM) have low nitrate concentrations.[17] Therefore, electrochemical low concentrated nitrate reduction is demanding because the faradaic efficiency decreases dramatically when the nitrate concentration is below 10 mM due to nitrate diffusion and the kinetically competitive HER reaction.[18] Secondly, a high operating voltage needs to be applied to the solution in order to achieve a sufficiently high catalytic NH_3 production. Nitrate reduction is a complex 8-electron reaction involving several intermediates (*e.g.*, NO_2 and NO) and slow multi-electron mediated reaction rates. Decentralised remote production of green ammonia from diluted aqueous nitrate solutions could be realised by developing an advanced electrode system to deliver high energy efficiency, selectivity and NO_3^- conversion rate using renewal electricity.

Advanced electrodes based on noble metals (*e.g.* Pd and Ru) have been explored as NitRR electrocatalysts,[19,20] however, their high price and abundance limits their large-scale application. Recent electrocatalysts have focused on earth-abundant transition metal in order to overcome the inherent disadvantages of noble metal-based electrocatalysts. However, most of the transition metals have their own inherent problems because NO_3^- has typically a low binding affinity for transition metals in an aqueous solution.[21,22] Moreover, the transition metals are more likely to form M–H bonds for competitive HER, leading to low selectivity and low catalytic efficiency for NitRR.[23] Significantly, copper metal catalysts have favorable binding energy for NO_3^- due to favourable energy level match between Cu's d-orbitals and nitrate's LUMO π^* molecular orbital.[24] Furthermore, the surfaces of Cu metal catalysts suppress HER and promote electron transfer, catalysing NO_3^- to NO_2^- conversion which is a rate-determining step of electrochemical nitrate reduction.[25] Nevertheless, Cu metal catalysts commonly undergo rapid deactivation owing to their strong adsorption of NitRR intermediates ($*NO_3$, $*NO_2$, *NO, *N, *NH and $*NH_2$), thus suppressing the further electrochemical reduction to NH_3.

In this context, hydrogen radical supplier mediated Cu metal electrocatalysts could be a novel solution to address the high NO_3^- concentration issues and the disadvantages of Cu metal by separating the sites of hydrogen radical formation and the sites of nitrate reduction because hydrogen radicals can reduce NitRR intermediates on selectively NO_3^--adsorbed Cu surface. As an active NitRR site, the highly porous Cu foam electrode is utilised both as a reduction reaction site enabling the selective NO_3^- adsorption on its surface at low NO_3^- concentrations and as an electrical conductor decreasing the materials cost for large-scale application. This compares favourably to electrodes that utilise nickel foam or carbon based substrates (carbon paper, carbon cloth) that only act as electrical conductors.[10,13–16,18,23,24,43–45,47,48,53] As a hydrogen radical supplier, layered double hydroxides (LDH; $\left[M_{1-x}^{2+}M'^{3+}_x(OH)_2\right]^{x+}(A^{n-})_{x/n}\cdot mH_2O$) could be a unique catalyst platform because of its high overpotential for HER if the Heyrovsky step ($H_{ads}* + H_2O + e^- \rightarrow H_2 + OH$) would be suppressed and if the Volmer step ($H_2O + e^- \rightarrow H_{ads}* + OH^-$) would be activated. Very few articles have been reported on electrochemical NitRR using an LDH because high voltage should require to drive the cathodic reaction in order to overcome the low inherent electrical conductivity. To date, few LDHs have been used as active materials in electrochemical NitRR, in each case both a high voltage and high nitrate concentration were needed to achieve a high FE which decreases the overall energy efficiency (*i.e.* $[NO_3^-] = 14$ mM $[NO_3^-]$ for Co_1Fe–CO_3 LDH;[43] $[NO_3^-] = 25$ mM for Cu_2CoAl–CO_3 LDH;[52] $[NO_3^-] = 100$ mM for Co_3AlCO_3 LDH[53]). In this work, we have explored a range of designer LDH decorated Cu foam electrodes (LDH/Cu foam) in order to investigate the role of mixed transition metal combinations to generate hydrogen radicals. We have prepared 12 LDH/Cu foam samples (LDHs = Ni_3Al–CO_3, Ni_3V–CO_3, Ni_3Fe–CO_3, Ni_3Co–CO_3, Co_3Al–CO_3, Co_3V–CO_3, Co_3Fe–CO_3, Zn_3Al–CO_3, Zn_3V–CO_3, Zn_3Fe–CO_3, Mg_3Al–CO_3 and Mg_3Fe–CO_3) which are representative active elements in electrocatalysts and evaluated them for electrochemical NitRR. The ultimate aim of the work is to increase the energy efficiency for selective nitrate reduction at low NO_3^- concentration. We found that the Ni_3Fe–CO_3 LDH/Cu foam electrode achieved the best electrochemical NitRR producing a 95.8% NH_3 selectivity with a 98.5% NO_3^- conversion in 5 mM NO_3^-. Over 1 h the system exhibited a NH_3 productivity of 1.261 mg cm^{-2} h^{-1} and a 96.8% FE at -0.2 V. This equates to a 36.6% half-cell energy efficiency. As far as we are aware, this is the highest energy efficient electrochemical NitRR to date.

2 Results and discussion

A hybrid LDH-Cu foam electrode for electrochemical nitrate reduction is illustrated in Fig. 1(a), where hydrogen radicals produced from water by a LDH are transferred to a Cu foam surface for electrochemical NitRR. LDHs adopt a brucite-like layered structure with cationic and anionic layers. The positively charged metal cationic layers ($\left[M_{1-x}^{2+}M'^{3+}_x(OH)_2\right]^{x+}$) are balanced by solvated anionic layers (A^{n-}) as shown in Fig. S1 (ESI†).[28] Powder X-ray Diffraction (PXRD) patterns for 12 LDHs with different combinations of metal cations (M^{2+}: Ni, Co, Zn, Mg and $M'^{(3+x)+}$: Al, Fe, Co, V) are shown in Fig. S2 (ESI†), the materials show the Bragg reflections at $2\theta = 11^\circ$ and 22° that can be indexed as (003) and (006) reflections for a prototypical LDH unit cell. In Table S1 (ESI†), calculated interlayer distance

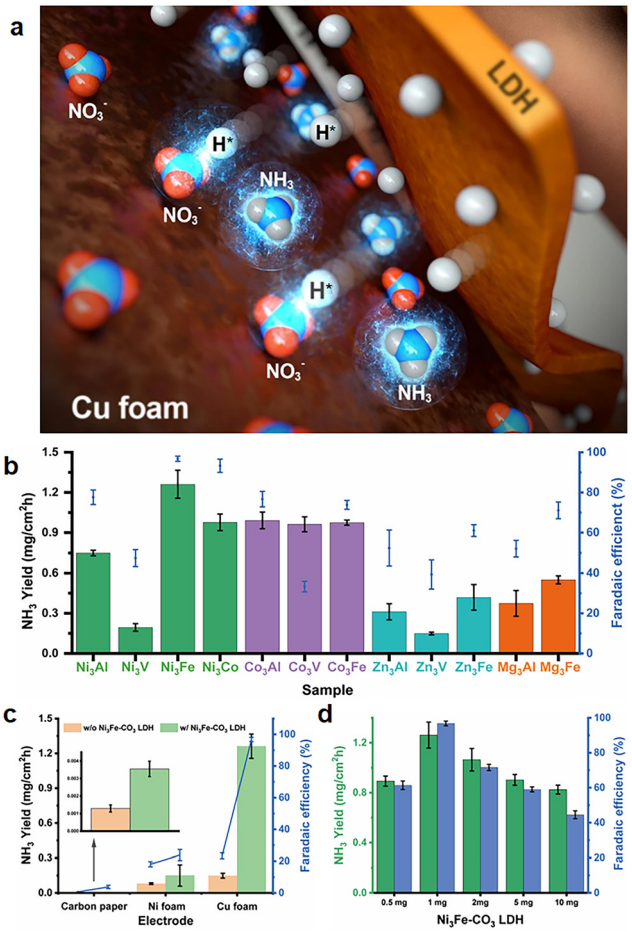

Fig. 1 Layered double hydroxide-Cu foam electrochemical nitrate reduction. (a) Schematic illustration of a hybrid multi-metallic LDH modified Cu foam electrode for electrochemical nitrate reduction, where hydrogen radicals produced and transferred to nitrate adsorbed on Cu foam surface by a LDH in an aqueous solution. (b) NH_3 productivity (mg cm^{-2} h^{-1}) and faradaic efficiency (%) using multi-metallic transition metal LDH/Cu foam electrodes. (c) NH_3 productivity and faradaic efficiency (%) using the electrodes w/and w/o $Ni_3Fe–CO_3$ LDH. (d) The effect of $Ni_3Fe–CO_3$ LDH loading on NH_3 productivity and faradaic efficiency. All electrocatalysis reactions was operated at 1 M KOH electrolyte with 5 mM of KNO_3 at −0.2 V (*vs.* RHE).

(d_{003}) and lattice parameters correspond to a hydrotalcite-3R type LDH with the *R3m* symmetry.

Twelve LDHs were prepared to investigate the optimum transition metal combinations for the hydrogen radical supplier role, and electrochemical NitRR was conducted for an hour using a chronoamperometric technique with an LDH/Cu foam electrode as a working electrode, applying a −0.2 V potential in 1 M KOH electrolyte with 5 mM KNO_3. As shown in Fig. 1(b), the Ni and Co based LDHs show relatively higher yield and FE than the Zn and Mg based LDHs except for the V containing LDHs because V ions in the LDH were active sites for HER suppressing NH_3 production. In the case of $Zn_3Fe–CO_3$ and $Zn_3V–CO_3$ LDH, ZnO phase was mixed with LDH phase. To clarify the ZnO effect, we have measured electrochemical NitRR of pure ZnO (Fig. S3, ESI†). It was found out that pure ZnO has similar properties compared to $Zn_3Fe–CO_3$ and $Zn_3V–CO_3$ LDH, which is not proper candidate for electrochemical NitRR. Among the twelve types of LDH, the $Ni_3Fe–CO_3$ LDH/Cu foam electrode exhibits the highest catalytic activity with a yield rate of 1.261 mg cm^{-2} h^{-1} and 96.8% of a FE from NO_3^- to NH_3, at −0.2 V. The hydrogen radical supplier role of the LDH was confirmed in Fig. 1(c), showing NH_3 yield rate and FE depending on the electrode type and the presence of the $Ni_3Fe–CO_3$ LDH. When carbon paper (CP) is utilised as an electrode, the conversion and FE for NH_3 production are neglectable regardless of the $Ni_3Fe–CO_3$ LDH because both CP and $Ni_3Fe–CO_3$ LDH are not the active sites for electrochemical NO_3^- reduction. In the case of the Ni foam electrode, a yield rate (and FE) before and after introducing the $Ni_3Fe–CO_3$ LDH on the surface of Ni foam electrode exhibit 0.080 mg cm^{-2} h^{-1} (18.1%) and 0.150 (23.8%) mg cm^{-2} h^{-1}, respectively. The Ni foam electrode has an inherent activity for electrochemical NitRR, however, the formation of Ni–H bonds facilitates competitive HER, leading to a low yield and low FE. Introducing the $Ni_3Fe–CO_3$ LDH onto a Ni foam surface leads to a slight increase in NH_3 production rate and FE. A Cu foam electrode displays a NH_3 production rate of 0.149 mg cm^{-2} h^{-1} which is approximately 1.9 times higher than that of the Ni foam. This supports the hypothesis that Cu foam has more favorable active sites for electrochemical NitRR. Nonetheless, the FE of 23.4% for a Cu foam is very similar to that of Ni foam, implying that N-containing intermediate poisoning (*NO_3, *NO_2, *NO, *N, *NH and *NH_2) during NitRR suppresses NH_3 production because Cu has selective *NO_3 adsorption followed by unfavourable ΔG for *NO_2 adsorption.[58,59] Remarkably, the NH_3 production rate improved more than 8.5 times and the FE reached 96.8% by introducing $Ni_3Fe–CO_3$ LDH onto the Cu foam surface. As the $Ni_3Fe–CO_3$ LDH proved to be inactive for NitRR, it mainly acts as a hydrogen radical supplying role during the electrochemical reaction. Surface coverage effects with $Ni_3Fe–CO_3$ LDH were revealed in Fig. 1(d). The amount of $Ni_3Fe–CO_3$ LDH loading on the foam was varied from 0.5 mg to 10 mg, we observed a volcanic dependence for both yield rate and FE as a function of LDH loading. Maximum electrocatalytic performance was observed at a loading of 1 mg. We suggest this is due to the LDH particles blocking NO_3^- access to the active Cu surface.

To further understand the $Ni_3Fe–CO_3$ LDH/Cu foam electrode, the structure of $Ni_3Fe–CO_3$ LDH was analysed by PXRD and Fourier transform-infrared (FT-IR) spectroscopy. The PXRD (Fig. 2(a)) contains a series of basal and non-basal plane Bragg reflections which demonstrate the highly crystalline nature of the LDH phases.[28] The interlayer anions can be identified as CO_3^{2-} by the asymmetric stretching band for CO_3^{2-} at around 1357 cm^{-1} in the FT-IR (Fig. S4, ESI†). Additionally, two absorbances found at around 3800–2600 cm^{-1} and at 1635 cm^{-1} can be ascribed to the stretching modes of the hydrogen-bonded HO···H_2O interactions and the angular deformation of the interlayer H_2O respectively.[29] The thermogravimetric analysis (TGA) shows the typical two step weight loss profile for an LDH (Fig. S5, ESI†). The desorption of water in the interlayer

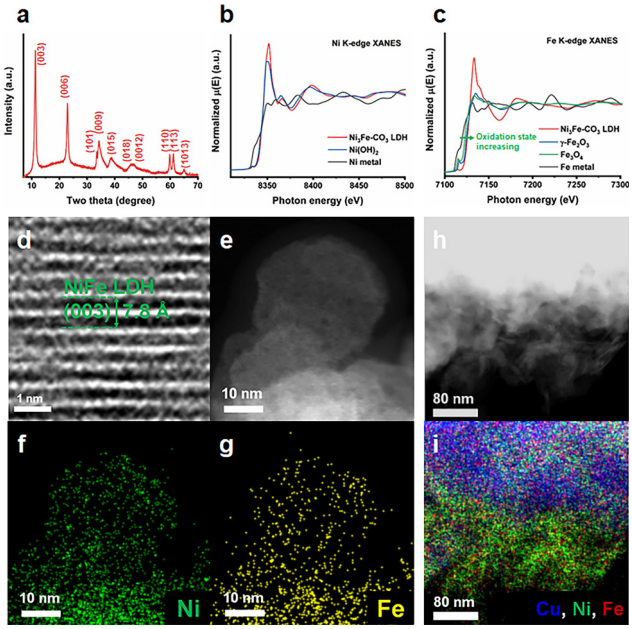

Fig. 2 Structural studies of electrocatalysts: (a) PXRD of $Ni_3Fe–CO_3$ LDH, (b) Ni K-edge XANES $Ni_3Fe–CO_3$ LDH with suitable reference materials, (c) Fe K-edge XANES of $Ni_3Fe–CO_3$ LDH with suitable reference materials, (d) HR-TEM image of $Ni_3Fe–CO_3$ LDH, (e) HAADF-STEM image of $Ni_3Fe–CO_3$ LDH, (f) STEM Ni mapping image of $Ni_3Fe–CO_3$ LDH, (g) STEM Fe mapping image for $Ni_3Fe–CO_3$ LDH, (h) a HAADF-STEM image, (i) STEM Cu, Ni, Fe mapping image for the $Ni_3Fe–CO_3$ LDH/Cu foam electrode.

region occurs below 200 °C, and the LDH structure collapses due to dehydration of hydroxyl ions on the cationic layers and the pyrolysis of anions in the interlayers between 200 °C and 400 °C.[30] The X-ray absorption spectroscopy (XAS) were conducted to probe the local electronic structure around Ni and Fe cations in $Ni_3Fe–CO_3$ LDH. The valence state of Ni in $Ni_3Fe–CO_3$ LDH was revealed by comparing the Ni K-edge X-ray absorption near-edge spectroscopy (XANES) spectra of $Ni(OH)_2$ and Ni metal (Fig. 2(b)). The Ni K-edge XANES spectra show a strong absorption edge at approximately 8350 eV, implying that Ni ions are divalent. Both $Ni_3Fe–CO_3$ LDH and $Ni(OH)_2$ have similar shape spectra with absorption edges at around 8350 eV.[31] The Fourier transformed extended X-ray absorption fine structure (FT-EXAFS) spectra were analysed to elucidate the coordination sphere of Ni. $Ni_3Fe–CO_3$ LDH and $Ni(OH)_2$ exhibit the same radial Ni–O bonding at 1.56 Å (Fig. S6a, ESI†). However, the radial distance for Ni–metal bonding in $Ni_3Fe–CO_3$ LDH (2.70 Å) is slightly shorter than that of $Ni(OH)_2$ (2.76 Å). Ni metal has only Ni–Ni bonds at 2.17 Å, matching well with a previous study.[32] The Fe oxidation state and coordination environment were analysed using Fe K-edge XANES and FT-EXAFS. $Ni_3Fe–CO_3$ LDH contains trivalent Fe^{3+} (Fig. 2(c)), as evidenced by the rising edge position being right-shifted in the order of Fe metal (Fe^0), Fe_3O_4 (Fe^{2+} and Fe^{3+}), γ-Fe_2O_3 (Fe^{3+}) and $Ni_3Fe–CO_3$ LDH. The right-shifted absorption edge between Fe_3O_4 and γ-Fe_2O_3 is derived from Fe^{2+} ions occupying the octahedral sites in the inverse spinel structure of γ-Fe_2O_3. Moreover, the Fe K-edge FT-EXAFS indicates that $Ni_3Fe–CO_3$ LDH has Fe–O and Fe-metal distances of 1.56 Å and 2.67 Å respectively. We note that γ-Fe_2O_3 and Fe_3O_4 have slightly shifted bond lengths as a result of their different crystal structures compared to $Ni_3Fe–CO_3$ LDH. (Fig. S6b, ESI†). Transmission electron microscopy (TEM) confirmed the morphology of $Ni_3Fe–CO_3$ LDH. As shown in Fig. S7a (ESI†), $Ni_3Fe–CO_3$ LDH has a nanoplatelet morphology with a platelet diameter below 50 nm. The high-resolution transmission electron microscopy (HR-TEM) image (Fig. 2(d)), exhibits lattice fringes of 0.78 nm corresponding to the (003) Bragg reflection of the $Ni_3Fe–CO_3$ LDH from a platelet with a 5–7 nm thickness (Fig. S7b, ESI†). The high angle annular dark field (HAADF)-scanning transmission electron microscopy (STEM) image (Fig. 2(e)) and STEM-energy dispersive spectrometer (EDS) analysis (Fig. 2(f) and (g)) provides clear evidence that Ni and Fe are well-dispersed. The $Ni_3Fe–CO_3$ LDH/Cu foam electrode was also characterised by HAADF-STEM image and STEM-EDS mapping, showing that $Ni_3Fe–CO_3$ LDH is well-attached to Cu foam surface (Fig. 2(h) and 2(i)). The N_2 isotherm for $Ni_3Fe–CO_3$ LDH is categorised as type-4 with a BET specific surface area of 59.9 $m^2\ g^{-1}$, the pore size distribution is presented in Fig. S8a and b (ESI†).[32]

We investigated the electrochemical performance in NitRR and evaluated the synergistic effects between $Ni_3Fe–CO_3$ LDH and Cu foam at ambient conditions. The electrocatalysis was performed by a three-electrode system using Hg/HgO as the reference electrode, coiled platinum wire as the counter electrode, and $Ni_3Fe–CO_3$ LDH deposited on a Cu foam as the working electrode assembled with a H-type cell under 1 M KOH electrolyte with/without NO_3^- ions. High-purity argon gas was bubbled into the cathodic chamber during electro-reduction to prevent possible side-competitive reactions such as NRR. The NO_2^- and NH_3 concentrations were quantified using a colourimetric method (Fig. S9a–d, ESI†). Firstly, linear weep voltammetry (LSV) experiments were conducted to assess NitRR activity of the $Ni_3Fe–CO_3$ LDH/Cu foam electrode at different nitrate concentrations at a scan rate of 5 mV s^{-1} (Fig. 3(a)). Electrocatalytic reduction on Cu surfaces involves four main reactions denoted A1–A4.[33]

$$\text{A1: } NO_3^- + H_2O + 2e^- \rightarrow NO_2^- + 2OH^- \quad (1)$$

$$\text{A2: } NO_2^- + 4H_2O + 4e^- \rightarrow NH_2OH + 5OH^- \quad (2)$$

$$\text{A3: } NO_2^- + 5H_2O + 6e^- \rightarrow NH_3 + 7OH^- \quad (3)$$

$$\text{A4: HER from competing adsorption of H*} \quad (4)$$

The current density increased with the NO_3^- concentration, implying the $Ni_3Fe–CO_3$ LDH/Cu foam was electrocatalytically active for NitRR. Especially, current density is enhanced massively at A3 because the electrode specially facilitates the conversion of NO_3^- into NH_3 compared to other reduction reactions. In Fig. S10 (ESI†), Cu foam also has the NitRR activity determined by the current density difference between the absence and presence of nitrate. However, the maximum current density (−42.8 mA cm^{-2}) at A3 is significantly lower than that of −79.4 mA cm^{-2} after $Ni_3Fe–CO_3$ LDH incorporation with 5 mM NO_3^- condition. In accordance with LSV curves,

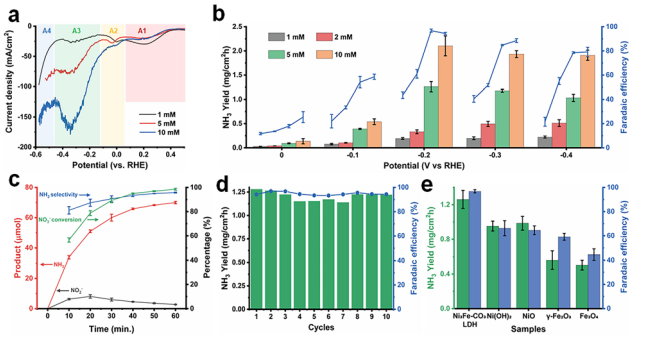

Fig. 3 Electrochemical performance of the $Ni_3Fe–CO_3$ LDH LDH/Cu foam electrode. (a) Linear sweep voltammetry (LSV) of the $Ni_3Fe–CO_3$ LDH LDH/Cu foam electrode depending on the different KNO_3 concentration. The scan rate of LSV is 5 mV s^{-1}. A1: $NO_3^- + H_2O + 2e^- \rightarrow NO_2^- + 2OH^-$, A2: $NO_2^- + 4H_2O + 4e^- \rightarrow NH_2OH + 5OH^-$, A3: $NO_2^- + 5H_2O + 6e^- \rightarrow NH_3 + 7OH^-$, A4: HER from competing adsorption of H* (b) NH_3 productivity and faradaic efficiency as a function of KNO_3 concentration and applied potential. (c) Calculated NH_3 selectivity, NO_3^- conversion and the amount of NH_3 and NO_2^- production as a function of time (d) NH_3 production rate and faradaic efficiency as a function of cycle number. (e) Comparison of NH_3 productivity and faradaic efficiency with those of selected reference materials for an hour using chronoamperometric analysis. In (c)–(e), the potential was applied to −0.2 V (*vs.* RHE) at 1 M KOH with 5 mM of KNO_3. All electrochemical reactions were conducted using the $Ni_3Fe–CO_3$ LDH/Cu foam electrode (1 mg cm^{-2}) in 1 M KOH electrolyte.

NH_3 productivity and FE for $Ni_3Fe–CO_3$ LDH/Cu foam electrode were measured as a function of NO_3^- concentrations (1 mM, 2 mM, 5 mM and 10 mM) at applied voltages from 0 V to −0.4 V as shown in Fig. 3(b). Each reaction was conducted using the chronoamperometric method for 1 h in 15 mL electrolyte containing 1 M KOH. The NH_3 yield increases with the decreasing potential until −0.2 V for all nitrate concentrations. When a more negative potential than −0.2 V is applied, the NH_3 productivity drops slightly because of competition with HER. Furthermore, NO_3^- conversion rates are very fast with most of the NO_3^- converted within an hour for all NO_3^- concentrations, up to a maximum of 98.5% in 5 mM [NO_3^-]. The rapid kinetics is illustrated by a decrease in current density within an hour (Fig. S11, ESI†). The FE was observed to vary as a function of NO_3^- concentrations and applied voltage (Fig. 3(b)). There was little change as a function of NO_3^- concentrations at 0 V which is attributed to lack of reduction energy. When the reduction voltage was between −0.1 V to −0.4 V, it was found that the FE was nearly linearly dependent on the NO_3^- concentration until it reached 5 mM and then saturated. This suggests first-order reaction kinetics at NO_3^- concentrations below 5 mM. The FE reached maximum values at −0.2 V and decreased at more negative voltages. This is a consequence of a competitive HER becoming active over −0.2 V at all NO_3^- concentrations. We found that the FE can reach 96.8% in 5 mM at −0.2 V, which represents a 36.6% energy-efficiency for conversion of NO_3^- to NH_3. The evolved products were analysed every 10 min at 5 mM NO_3^- and −0.2 V. Both NH_3 and NO_2 evolved within 10 min (Fig. 3(c)) with 56.5% NO_3^- conversion. After 10 minutes, the quantity of NO_2 decreased while NH_3 increased gradually reaching 95.8% NH_3 selectivity and 98.5% of NO_3^- conversion after 60 min. Neither H_2 nor N_2 was detected during the electrochemical reaction using a gas chromatography (GC) equipped with a capillary column and mass selective detector (MSD), indicating no HER or nitrification reactions are taking place. However, the concentration of the initial 74.2 μmol NO_3^- source rapidly reduced to zero after 60 min, only NO_3^-, NO_2^- and NH_3 can be determined during electrochemical NitRR. (Fig. S12a, ESI†) Moreover, LSV curves (Fig. S12b, ESI†) shows that most of electrochemical reduction reactions finished after 50 min, which matched well with the time-dependent analysis of products in Fig. S12a (ESI†). The $Ni_3Fe–CO_3$ LDH/Cu foam electrode exhibited excellent stability as shown in Fig. 3(d), sustaining a NH_3 productivity of >1.138 mg cm^{-2} h^{-1}, and a FE of >93.3% after 10 cycles of operation in 5 mM NO_3^- at −0.2 V. The role of Ni and Fe in the $Ni_3Fe–CO_3$ LDH/Cu foam electrode during electrochemical NitRR was investigated by looking at other related reference materials including $Ni(OH)_2$, NiO, γ-Fe_2O_3 and Fe_3O_4 on Cu foam. As a hydrogen radical supplier in electrochemical NitRR two processes need to be optimised, the kinetic energy barrier for the Volmer reaction should be matched with the potential range for NO_3^- reduction. If the energy barrier is too low, a chain reaction will occur leading to HER. Meanwhile, if the energy barrier is too high, water will not be dissociated into hydrogen radicals. In addition, the Heyrovsky reaction should be suppressed to prevent H–H bond formation during electrochemical NitRR. In this regard, $Ni_3Fe–CO_3$ LDH is an ideal candidate as a hydrogen radical supplier because of having a high kinetic energy barrier for the Volmer reaction (HER overpotential of >210 mV at 10 mA cm^{-2}) and a rate-limiting Heyrovsky reaction which prevents H–H formation during electrochemical NitRR.[26,27] Fig. 3(e) shows that $Ni(OH)_2$ and NiO result in high NH_3 production rate of 0.952 mg cm^{-2} h^{-1} and 0.985 mg cm^{-2} h^{-1}, respectively, which are comparable to that of $Ni_3Fe–CO_3$ LDH. However, their FE of 66.3% and 64.6% are significantly lower than that of the $Ni_3Fe–CO_3$ LDH. We postulate that Ni oxide-based materials could produce and transfer hydrogen radicals facilitating electrochemical NitRR on a Cu surface. However, it still provides an available surface for the Tafel reaction – H_2 production *via* adsorbed hydrogen facilitated on a Ni–O–Ni surface results in a decreased FE.[34,35] In the case of Fe oxide-based materials, both γ-Fe_2O_3 and Fe_3O_4 have lower NH_3 productivity and FE, meaning the absence of active production and transfer abilities for hydrogen radicals due to low Fe–H binding energy compared to Ni–H bonding.[36,37] Remarkably, the $Ni_3Fe–CO_3$ LDH had both Ni hydroxide layers facilitating the production of hydrogen radicals and Fe heteroatoms transferring hydrogen radicals to Cu sites by decreasing the bonding energy of metal–H bonding and inhibiting the Tafel step, thereby enabling the high yield rate and FE in electrochemical NitRR.

Ex situ XAS and X-ray photon spectroscopy (XPS) were performed to elucidate the bulk and surface structural changes of the $Ni_3Fe–CO_3$ LDH/Cu foam electrode before and after electrochemical NitRR. Wavelet transformed (WT)-EXAFS were

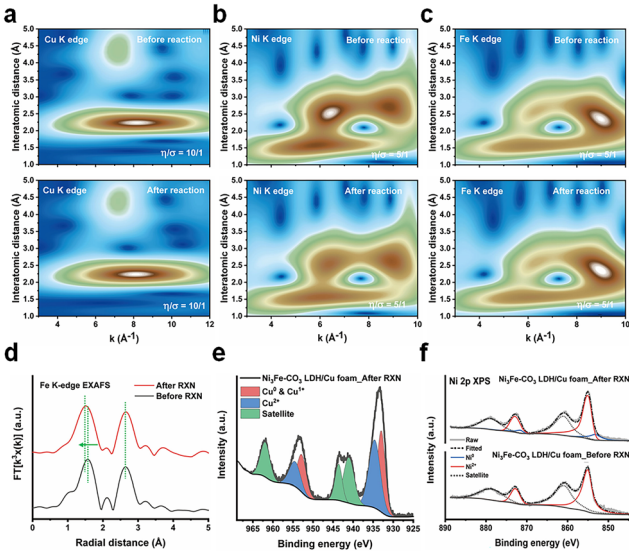

Fig. 4 X-Ray spectroscopic studies of electrocatalyst before and after electrochemical NO_3^- reduction. (a) Cu K-edge XAS, (b) Ni K-edge XAS, and (c) Fe K-edge WT-EXAFS before and after electrochemical NitRR for the $Ni_3Fe–CO_3$ LDH/Cu foam. (d) Fe K-edge EXAFS of the $Ni_3Fe–CO_3$ LDH/Cu foam electrode, and (e) Cu 2p XPS of the $Ni_3Fe–CO_3$ LDH/Cu foam electrode after electrochemical NitRR. (f) Ni 2p XPS of $Ni_3Fe–CO_3$ LDH/Cu foam electrodes before and after the electrochemical NitRR. RXN means electrochemical NitRR and after RXN sample has analysed after 1 cycle of the electrochemical reaction conducted by chronoamperometric technique for an hour at −0.2 V (*vs.* RHE) in 1 M KOH with 5 mM of KNO_3.

analyzed to confirm the EXAFS structure both in k and r space simultaneously.[38] The Cu K-edge WT-EXAFS shows only two main maxima identified by Cu–Cu scattering of the first shell at $k \approx 8.17$ Å^{-1} and $R \approx 2.24$ Å and by Cu–Cu scattering of the second shell at $k \approx 7.16$ Å^{-1} and $R \approx 4.40$ Å as shown in Fig. 4(a). Additionally, the Cu K-edge XANES (Fig. S13a, ESI†) and FT-EXAFS (Fig. S13b, ESI†) did not change, indicating the bulk structure of the Cu foam remains after the reaction. The $Ni_3Fe–CO_3$ LDH also retains its bulk structure after reaction as determined by Ni K-edge (WT-EXAFS in Fig. 4(b), XANES in Fig. S14a (ESI†) and FT-EXAFS in Fig. S14b, ESI†) and Fe K-edge (WT-EXAFS in Fig. 4(c) and XANES in Fig. S15, ESI†). However, the 1st Fe–O shell changed from 1.57 Å to 1.53 Å after electrochemical NitRR (Fig. 4(d)), suggesting that Fe affects the hydrogen radical transfer owing to lower binding strength of hydrogen to a Fe^{3+} centre.[37] Using XPS analysis, a more significant change can be observed on the surface structure after NO_3^- reduction compared to that of the bulk structure. The Cu 2p XPS indicated Cu in the $Ni_3Fe–CO_3$ LDH/Cu foam is metallic before the reaction (Fig. S16, ESI†), however, after NO_3^- reduction both Cu_2O and CuO phases were detected (Fig. 4(e)). This indicated that *in situ* electrochemical reconstruction occurs during the electrochemical reaction on its surface, by forming the Cu/Cu_2O interface resulting in *NOH reaction, thus becoming an additional benefit for a high NH_3 selectivity.[39] Furthermore, the XPS data reveal that both Ni^{2+} (Fig. 4(f)) and Fe^{3+} (Fig. S17, ESI†) cations were reduced after the reaction. We observe the formation of metallic Ni on the $Ni_3Fe–CO_3$ LDH surface after NitRR. This suggests that $Ni_3Fe–CO_3$ LDH promote hydrogen radical transfer by hydrogen spillover mechanism.[40] This surface reduction can also be observed by cyclic voltammetry (CV) of $Ni_3Fe–CO_3$/Cu foam and Cu foam. The curves show that new reduction and oxidation events take place depending on the direction of the applied potential upon introduction of $Ni_3Fe–CO_3$ LDH in the 1 M KOH. This indicates that the surface of LDH can be reduced during electrochemical NitRR (Fig. S18, ESI†). Nevertheless, we observe stable performance as the bulk structure of these materials is maintained despite surface changes during the electrochemical processes. Several electrochemical and spectro-electrochemical techniques were used in order to further elaborate the role of $Ni_3Fe–CO_3$ LDH in electrochemical NitRR (Fig. 5). Firstly, the electrochemically active surface area (ECSA) was obtained by determining the electrochemical double-layer capacitance (C_{dl}) from CV at various scan rates as shown in Fig. 5(a). In 1 M KOH without NO_3^-, the $Ni_3Fe–CO_3$ LDH/Cu foam electrode shows 2.29 mF cm^{-2} of C_{dl} which is 2.77 times higher than that of the Cu foam electrode. This indicated that both H_2O and OH^- could be adsorbed actively on $Ni_3Fe–CO_3$ LDH rather than on a Cu surface. Whereas in 1 M KOH with 5 mM KNO_3, the C_{dl} of the Cu foam electrode increased 2.45 times implying that most NO_3^- adsorbs on the Cu surface because the C_{dl} of the $Ni_3Fe–CO_3$ LDH with or without NO_3^- is the same. Secondly, the charge transfer characteristics were studied using potentiostatic electrochemical impedance spectroscopy (pEIS) in 1 M KOH with 5 mM KNO_3 electrolyte at −0.2 V, fitted by a proper equivalent circuit having the series resistance ($R1$), Cu foam/electrolyte resistance ($R2$), and the $Ni_3Fe–CO_3$ LDH/electrolyte interface resistance ($R3$) as shown in Fig. 5(b) and Table S2 (ESI†). It is found that the R_2 value (0.277 Ω) for the $Ni_3Fe–CO_3$ LDH/Cu foam electrode is about 13.5 times lower than that for the Cu foam electrode (3.658 Ω), indicating that the charge transfer characteristics are significantly enhanced by hydrogen radical supply from $Ni_3Fe–CO_3$ LDH. Thirdly, electron spin resonance (ESR) spectroscopy was carried out to confirm the production of hydrogen radicals during elecectrochemical NitRR (Fig. 5(c)). To capture these unstable radical species, a chronoampherometric measurement was carried out using 50 mM 5,5-dimethyl-1-pyrroline-*N*-oxide (DMPO) in 1 M KOH electrolyte at –0.2 V. Regardless of the $Ni_3Fe–CO_3$ LDH, both spectra have superoxide (O_2^-) radicals generated from dissolved oxygen molecules in the KOH electrolyte. However, the ESR signal of hydrogen radicals was observed when the $Ni_3Fe–CO_3$ LDH is introduced onto the Cu surface, providing direct evidence for the hydrogen radical generating capability of $Ni_3Fe–CO_3$ LDH.[41] To determine the kinetics regarding hydrogen radical generation and transfer to $Ni_3Fe–CO_3$ LDH/Cu foam electrode, the Tafel plots were analysed under HER conditions of 1 M KOH electrolyte (Fig. S19, ESI†). In principle, if the Volmer step is rate-determining for the overall reaction rate, adsorbed hydrogen radicals would be consumed quickly by the faster Heyrovsky and/or Tafel step on the surface of electrode. It means that the Tafel slope has single value because the reaction is limited by hydrogen coverage.

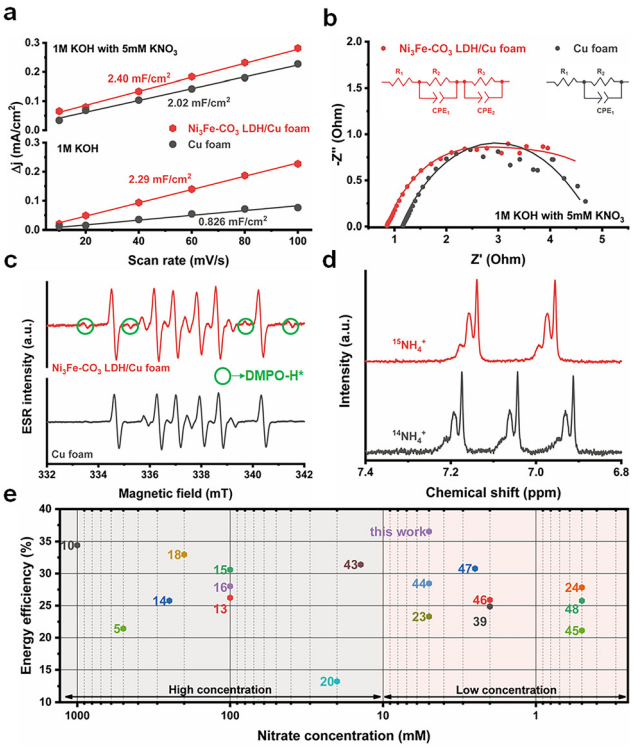

Fig. 5 (a) Double layer capacitance for the $Ni_3Fe–CO_3$ LDH/Cu foam and Cu foam electrodes with/without 5 mM KNO_3 in 1 M KOH electrolyte based on the cyclic voltammetry profiles at various scan rates. (b) The Nyquist plots for the EIS spectra of the $Ni_3Fe–CO_3$ LDH/Cu foam and Cu foam electrodes at −0.2 V (*vs.* RHE) under 1 M KOH with 5 mM KNO_3. (c) ESR spectra of the solutions obtained by the $Ni_3Fe–CO_3$ LDH/Cu foam and Cu foam electrodes in presence of 50 mM DMPO in 1 M KOH. The electrochemical reaction was conducted by chronoamperometric technique for an hour to trap the hydrogen radicals. (d) ^1H NMR spectra of the electrolyte after electrochemical NitRR using the $Ni_3Fe–CO_3$ LDH/Cu foam electrocatalyst at −0.2 V (*vs.* RHE) using $K^{15}NO_3$ as a feedstock. The electrochemical reaction was conducted by chronoamperometric technique for an hour under 1 M KOH electrolyte. (e) Half-cell energy efficiencies of this work as a function of [NO_3^-] compared with the recently reported electrocatalysts (The number indicates cited reference). *X*-Axis (nitrate concentration) was $\log_{10}$-scaled. Data in Table S2 (ESI†).

On the other hand, if Heyrovsky step is the rate-determining step, the hydrogen radicals would fully cover the electrode surface resulting in the inflection of the Tafel slope.[56] In Fig. S19a (ESI†), the Tafel plots of Cu foam has a singular slope, meaning the rate-determining step is Volmer step. After incorporating $Ni_3Fe–CO_3$ LDH (Fig. S19b, ESI†), the Tafel slope of electrode has an inflection depending on the negative overpotential. This means the overall rate cannot increase fast enough because the surface adsorption of hydrogen radicals has been fully saturated.[57] From this kinetics analysis, $Ni_3Fe–CO_3$ LDH/Cu foam electrode can generate hydrogen radicals at negative potential, but Cu foam cannot because of rate-determining Volmer reaction. Furthermore, radical trapped DMPO mediated ESR spectra of Ni foam, $Ni_3Fe–CO_3$/Ni foam, C paper and $Ni_3Fe–CO_3$/C paper has carried out to study the synergistic effect between $Ni_3Fe–CO_3$ LDH and Cu foam for hydrogen radical generation and transfer. In the case of $Ni_3Fe–CO_3$/Ni foam and Ni foam (Fig. S20a, ESI†), only small amount of superoxide radicals was observed, but none was observed using C paper and $Ni_3Fe–CO_3$/C paper (Fig. S19b, ESI†).[41] This is highly supportive of synergy between the $Ni_3Fe–CO_3$ and Cu foam when it comes to these hydrogen radicals mediated processes (Fig. S20c, ESI†). Lastly, a $K^{15}NO_3$ isotope experiment was performed to trace the origin of the NH_3 generated by chronoamperometric analysis both in 5 mM $K^{14}NO_3$ and $K^{15}NO_3$ electrolyte. In Fig. 5(d), the ^1H NMR spectrum exhibits a 1 : 1 : 1 triplet with a spacing of 52.2 Hz ascribed to $^{14}NH_4^+$. In the case of the $K^{15}NO_3$ electrolyte solution, the ^1H NMR spectrum shows clear doublet with a spacing of 73.1 Hz corresponding to $^{15}NH_4^+$, as a result of scalar interaction between ^1H and ^{15}N.[42] These observations confirm that NH_3 derives from NO_3^- dissolved in the solution phase. Fig. 5(e) and Table S3 (ESI†) provide a comparison of the half-cell energy efficiency of recently reported electrocatalysts and this work. It supports the claim that the half-cell energy efficiency of the $Ni_3Fe–CO_3$ LDH/Cu foam is superior to those of other recent electrocatalysts both at high and low NO_3^- concentrations, achieving 36.6% and 36.2% at 5 mM and 10 mM NO_3^- concentration respectively.[5,10,13–16,18,20,23,24,39,43–48]

3 Conclusions

In conclusion, we demonstrated robust and exceptional catalytic NitRR performance of a $Ni_3Fe–CO_3$ LDH/Cu foam electrode under low NO_3^- concentration. $Ni_3Fe–CO_3$ LDH/Cu foam exhibits 8.5-fold higher productivity compared to pristine Cu foam. Our electrocatalyst exhibits a 95.8% NH_3 selectivity at 98.5% NO_3^- conversion within an hour. A 36.6% of half-cell energy efficiency was achieved, while yielding a production rate of 1.261 mg cm^{-2} h^{-1} and 96.8% of FE at –0.2 V in 5 mM NO_3^-. These results support that the hybrid electrode structure offers both a highly porous Cu foam allowing the selective binding for NO_3^- and also a $Ni_3Fe–CO_3$ LDH coating facilitating hydrogen radical production/transfer, thus providing a new strategy for surface engineering involving hydrogen radicals in catalysis.

4 Experimental details

4.1. Preparation

Chemicals. The detailed chemicals are given in the ESI.†

Synthesis of layered double hydroxides. Layered double hydroxides (LDH) were synthesised by either co-precipitation or hydrothermal methods. The ratio of M^{2+} to M'^{3+} cations was 3 : 1 and all metal sources were MCl_2 and $M'Cl_3$ salts. In the case of $Ni_3Al–CO_3$, $Ni_3Fe–CO_3$, $Ni_3Co–CO_3$, $Co_3Al–CO_3$, $Co_3Fe–CO_3$, $Zn_3Al–CO_3$, $Mg_3Al–CO_3$ and $Mg_3Fe–CO_3$ a co-precipitation method was employed. For the $Ni_3Al–CO_3$ LDH, an aqueous solution of sodium carbonate (1.0 M) with sodium hydroxide (1.0 M) was pre-heated in a round flask at 60 °C. And then, 0.64 M of the metal precursors (0.48 M of $NiCl_2$ and 0.16 M of $AlCl_3$) was added to a pre-heated solution in a drop-wise manner. For $Ni_3Fe–CO_3$, $Ni_3Co–CO_3$, $Co_3Al–CO_3$, $Co_3Fe–CO_3$,

$Zn_3Al–CO_3$, and $Mg_3Al–CO_3$ after drop-wise addition, the reaction was heated for 24 h at 60 °C. The suspension produced was centrifugated several times at 6000 rpm for 10 min with water. Finally, the centrifugated powder was dried overnight at 30 °C in a vacuum oven. For the $Co_3V–CO_3$ LDH, an aqueous solution of sodium carbonate (1.0 M) with sodium hydroxide (1.0 M) was pre-heated in a round flask at 85 °C. And then, 0.64 M of the metal precursors (0.48 M of $CoCl_2$ and 0.16 M of VCl_3) were added to a pre-heated solution in a drop-wise manner. After drop-wise addition, the reaction was heated for 24 h at 85 °C. The suspension produced was centrifugated several times at 6000 rpm for 10 min with water. Finally, the $Co_3V–CO_3$ LDH powder was dried overnight at 30 °C in a vacuum oven. $Ni_3V–CO_3$, $Zn_3V–CO_3$ and $Zn_3Fe–CO_3$ LDHs were synthesised by a urea hydrolysis method. 0.04 M of metal precursor solution with 0.0625 M urea (80 mL of the total solution) was heated in the 125 mL Teflon-lined stainless-steel autoclave for 12 h at 120 °C. The suspension produced was centrifugated several times at 6000 rpm for 10 min with water. Finally, the pre-synthesised powder was dried overnight at 30 °C in a vacuum oven.

Preparation of the LDH/Cu foam electrode. First, an electrocatalyst ink was prepared for the fabrication of the electrode. 10 mg of as-prepared powder was dissolved into 1 mL of ethanol with 50 μL of perfluorinated resin solution containing Nafion™ 1100W. Second, a 2 cm × 1 cm Cu foam was cut before ultrasonication pre-cleaning with acetone, 3 M HCl and DI water in sequence for 15 min to remove any contamination and possible surface oxide layers. Then, 100 μL of as-prepared electrocatalyst ink (1 mg of LDH) was slowly deposited on 1 cm × 1 cm size of the Cu foam. Finally, the LDH/Cu foam electrode was dried at room temperature for 12 hours.

4.2. Electrochemical characterisation

Electrochemical measurements. All the electrochemical measurements were carried out using a Gamry (Reference 3000) workstation. The coiled Pt wire counter electrode and Hg/HgO reference electrode (filled with 1 M KOH) were used to measure electrochemical nitrate reduction properties in an H-type electrolytic cell separated by a Nafion-117 membrane. An aqueous electrolyte of 1 M KOH (pH 14) was used as an electrolyte, and KNO_3 was added into the cathode compartment (15 mL) as the reactant and continuously purged with Ar gas (99.999%) during NO_3^- reaction. Unless otherwise specified, the concentration of NO_3^- was 5 mM and chronoamperometric experiments are carried out for 1 h at a constant potential. The scan rate of the current–voltage curve was 5 mV s^{-1} and electrochemical impedance spectroscopy analysis was performed from 0.1 Hz to 0.1M Hz. The measured potentials (*vs.* the Hg/HgO) were converted into the reversible hydrogen electrode (V_{RHE}) scale by using the Nernst equation

$$V_{RHE} = V_{Hg/HgO} + 0.059 \times pH + V^{\circ}_{Hg/HgO\ vs.\ NHE}$$

where $V_{Hg/HgO}$ is the experimental penitential value against the Hg/HgO reference electrode, pH is 14 at a 1 M KOH aqueous solution and $V^{\circ}_{Hg/HgO\ vs.\ NHE}$ is 0.098 V at 25 °C. NO_3^- conversion (%), NH_3 selectivity (%), faradaic efficiency (%) and NH_3 productivity (mg cm^{-2} h^{-1}) were obtained using the following equations:

$$\text{Nitrate conversion (\%)} = \Delta C_{nitrate}/C_0 \times 100\%$$

$$\text{Ammonia selectivity (\%)} = C_{ammonia}/\Delta C_{nitrate} \times 100\%$$

$$\text{Faradaic efficiency (\%)} = (n \times F \times C_{ammonia} \times V)/(M \times Q)$$

$$\text{Ammonia productivity (mg cm}^{-2}\text{ h}^{-1}\text{)} = (C_{ammonia} \times V)/(t \times S)$$

where $\Delta C_{nitrate}$ is NO_3^- concentration difference between before and after the reaction; C_0 is the initial NO_3^- concentration; $C_{ammonia}$ is the concentration of NH_3 after reaction; n is the number of electrons to be used in respective reaction; F is the faradaic constant; V is the volume of the cathode compartment (0.015 L); M is the relative molecular mass; Q is the total charge used for electroreduction reaction; t is the reaction time (h); S is the geometric area of the electrode (1 cm^2).

Isotope-labelling experiment. The isotopically-labelled $K^{15}NO_3$ experiments were carried out to trace the source of ammonia during electrochemical nitrate reduction. The coiled Pt wire counter electrode and Hg/HgO reference electrode (filled with 1 M KOH) were used to measure electrochemical nitrate reduction performance with an H-type electrolytic cell separated by a Nafion-117 membrane using Gamry (Reference 3000) workstation. An aqueous electrolyte of 1 M KOH (pH 14) was used as an electrolyte with 5 mM of $K^{15}NO_3$ in the cathode compartment (15 mL) and Ar gas (99.999%) was continuously purged during a hour of reaction time at −0.2 V. After the reaction, 3.25 mL of solution in cathodic counterparts were extracted to mix with 1.5 mL of D_2O and 0.25 mL of dimethylsulfoxide (DMSO) before adjusting the pH to about 4 to 5 with 3 M HCl to detect the nitrogen source as ammonium ions. The as-prepared solution was analyzed by ^1H NMR for revealing the source of nitrogen in ammonia. Similarly, $K^{14}NO_3$ was used as the nitrogen source of $^{14}NO_3^-$ to compare with the ^{15}N isotope experiment.

Product detection. The amount of NH_3 produced was determined by colourimetry using the indophenol blue method.[49] 2 mL of the electrolyte was taken from the cathodic counterpart, and then, mixed with 2 mL of a 1 M NaOH solution containing 5 wt% of salicylic acid and 5 wt% of sodium citrate. Next, 1 mL of 0.05 M NaClO and 0.2 mL of 1 wt% $C_5FeN_6Na_2O$ (sodium nitroferricyanide) were added to the above solution before storing at room temperature for 2 h. The concentration of NH_3 can be detected at a wavelength of about 660 nm using the ultraviolet-visible absorption spectroscopy. The NO_2^- concentration was detected by dissolving 20 g of *p*-aminobenzenesulfonamide and 1 g of *N*-(1-naphthyl) ethylenediamine dihydrochloride into the mixture of 250 mL of DI water and 50 mL of phosphoric acid. Then, this solution was diluted to 500 mL of volume. This colouring agent solution was mixed with electrolyte from the cathodic counterpart. Finally, the concentration of NO_2^- can be detected at a wavelength of about 540 nm using the ultraviolet-visible absorption spectroscopy.[50]

The NO_3^- concentration was determined by adding 1 M HCl (0.2 mL) and 0.8 wt% sulfamic acid solution (0.02 mL) to the NO_3^- solution (10 mL). The absorption intensities at wavelengths of 220 and 275 nm were measured and calculated by the following equation[51] of '$A = A_{220nm} - 2A_{275nm}$.' A GC-MS (Agilent, GC-7890A and MS-5975C) equipped with a capillary column (Supleco, 30 m × 0.32 mm) and MSD (Mass selective detector, inert triple-axis detector) were used for gas phase product detection.

Conflicts of interest

The authors declare no conflict of interest.

Acknowledgements

This research was supported by the National Research Foundation of Korea (2022M3H4A1A04096482) funded by the Ministry of Science and ICT, and the Basic Science Research Program (2021R1A6A3A14044449) through the National Research Foundation of Korea funded by the Ministry of Education. We also thank SCG Chemicals Public Co. Ltd for support for a Fellowship to C. C.

Notes and references

1 Y. Ashida, K. Arashiba, K. Nakajima and Y. Nishibayashi, *Nature*, 2019, **568**, 536–540.
2 S. L. Foster, S. I. Perez Bakovic, R. D. Duda, S. Maheshwari, R. D. Milton, S. D. Minteer, M. J. Janik, J. N. Renner and L. F. Greenlee, *Nat. Catal.*, 2018, **1**, 490–500.
3 V. Rosca, M. Duca, M. T. de Groot and M. T. M. Koper, *Chem. Rev.*, 2009, **109**, 2209–2244.
4 R. F. Service, *Science*, 2014, **345**, 610.
5 Z.-Y. Wu, M. Karamad, X. Yong, Q. Huang, D. A. Cullen, P. Zhu, C. Xia, Q. Xiao, M. Shakouri, F.-Y. Chen, J. Y. Kim, Y. Xia, K. Heck, Y. Hu, M. S. Wong, Q. Li, I. Gates, S. Siahrostami and H. Wang, *Nat. Commun.*, 2021, **12**, 2870.
6 T. Kandemir, M. E. Schuster, A. Senyshyn, M. Behrens and R. Schlögl, *Angew. Chem., Int. Ed.*, 2013, **52**, 12723–12726.
7 S. Z. Andersen, V. Čolić, S. Yang, J. A. Schwalbe, A. C. Nielander, J. M. McEnaney, K. Enemark-Rasmussen, J. G. Baker, A. R. Singh, B. A. Rohr, M. J. Statt, S. J. Blair, S. Mezzavilla, J. Kibsgaard, P. C. K. Vesborg, M. Cargnello, S. F. Bent, T. F. Jaramillo, I. E. L. Stephens, J. K. Nørskov and I. Chorkendorff, *Nature*, 2019, **570**, 504–508.
8 C. Tang and S.-Z. Qiao, *Chem. Soc. Rev.*, 2019, **48**, 3166–3180.
9 X. Cui, C. Tang and Q. Zhang, *Adv. Energy Mater.*, 2018, **8**, 1800369.
10 S. Ye, Z. Chen, G. Zhang, W. Chen, C. Peng, X. Yang, L. Zheng, Y. Li, X. Ren, H. Cao, D. Xue, J. Qiu, Q. Zhang and J. Liu, *Energy Environ. Sci.*, 2022, **15**, 760–770.
11 Q. Hu, Y. Qin, X. Wang, Z. Wang, X. Huang, H. Zheng, K. Gao, H. Yang, P. Zhang, M. Shao and C. He, *Energy Environ. Sci.*, 2021, **14**, 4989–4997.
12 X. Deng, Y. Yang, L. Wang, X.-Z. Fu and J.-L. Luo, *Adv. Sci.*, 2021, **8**, 2004523.
13 X. Zhao, G. Hu, F. Tan, S. Zhang, X. Wang, X. Hu, A. V. Kuklin, G. V. Baryshnikov, H. Ågren, X. Zhou and H. Zhang, *J. Mater. Chem. A*, 2021, **9**, 23675–23686.
14 Y. Guo, R. Zhang, S. Zhang, Y. Zhao, Q. Yang, Z. Huang, B. Dong and C. Zhi, *Energy Environ. Sci.*, 2021, **14**, 3938–3944.
15 Z. Fang, Z. Jin, S. Tang, P. Li, P. Wu and G. Yu, *ACS Nano*, 2022, **16**, 1072–1081.
16 Q. Liu, L. Xie, J. Liang, Y. Ren, Y. Wang, L. Zhang, L. Yue, T. Li, Y. Luo, N. Li, B. Tang, Y. Liu, S. Gao, A. A. Alshehri, I. Shakir, P. O. Agboola, Q. Kong, Q. Wang, D. Ma and X. Sun, *Small*, 2022, **18**, 2106961.
17 P. H. van Langevelde, I. Katsounaros and M. T. M. Koper, *Joule*, 2021, **5**, 290–294.
18 J. Wang, C. Cai, Y. Wang, X. Yang, D. Wu, Y. Zhu, M. Li, M. Gu and M. Shao, *ACS Catal.*, 2021, **11**, 15135–15140.
19 J. Li, G. Zhan, J. Yang, F. Quan, C. Mao, Y. Liu, B. Wang, F. Lei, L. Li, A. W. M. Chan, L. Xu, Y. Shi, Y. Du, W. Hao, P. K. Wong, J. Wang, S.-X. Dou, L. Zhang and J. C. Yu, *J. Am. Chem. Soc.*, 2020, **142**, 7036–7046.
20 J. Lim, C.-Y. Liu, J. Park, Y.-H. Liu, T. P. Senftle, S. W. Lee and M. C. Hatzell, *ACS Catal.*, 2021, **11**, 7568–7577.
21 C. L. Ford, Y. J. Park, E. M. Matson, Z. Gordon and A. R. Fout, *Science*, 2016, **354**, 741–743.
22 W. He, J. Zhang, S. Dieckhöfer, S. Varhade, A. C. Brix, A. Lielpetere, S. Seisel, J. R. C. Junqueira and W. Schuhmann, *Nat. Commun.*, 2022, **13**, 1129.
23 S. Zhang, M. Li, Q. Song and X. Liu, *Proc. Natl. Acad. Sci. U. S. A.*, 2022, **119**, e2115504119.
24 Y. Xu, K. Ren, M. Wang, Z. Wang, X. Li, L. Wang and H. Wang, *Appl. Catal., B*, 2022, **306**, 121094.
25 Y. Wang, L. Zhang, Y. Niu, D. Fang, J. Wang, Q. Su and C. Wang, *Green Chem.*, 2021, **23**, 7594–7608.
26 G. Chen, T. Wang, J. Zhang, P. Liu, H. Sun, X. Zhuang, M. Chen and X. Feng, *Adv. Mater.*, 2018, **30**, 1706279.
27 A. Alobaid, C. Wang and R. A. Adomaitis, *J. Electrochem. Soc.*, 2018, **165**, J3395–J3404.
28 K.-H. Kim, S. Kim, B. C. Moon, J. W. Choi, H. M. Jeong, Y. Kwon, S. Kwon, H. S. Choi and J. K. Kang, *J. Mater. Chem. A*, 2017, **5**, 8274–8279.
29 K.-H. Kim, J. W. Choi, H. Lee, B. C. Moon, D. G. Park, W. H. Choi and J. K. Kang, *J. Mater. Chem. A*, 2018, **6**, 23283–23288.
30 A. Pastor, C. Chen, G. de Miguel, F. Martin, M. Cruz-Yusta, J.-C. Buffet, D. O'Hare, I. Pavlovic and L. Sánchez, *Chem. Eng. J.*, 2022, **429**, 132361.
31 W. E. O'Grady, K. I. Pandya, K. E. Swider and D. A. Corrigan, *J. Electrochem. Soc.*, 1996, **143**, 1613–1617.
32 M. Xu, S. Yao, D. Rao, Y. Niu, N. Liu, M. Peng, P. Zhai, Y. Man, L. Zheng, B. Wang, B. Zhang, D. Ma and M. Wei, *J. Am. Chem. Soc.*, 2018, **140**, 11241–11251.
33 X. Fu, X. Zhao, X. Hu, K. He, Y. Yu, T. Li, Q. Tu, X. Qian, Q. Yue, M. R. Wasielewski and Y. Kang, *Appl. Mater. Today*, 2020, **19**, 100620.

34 N. S. Gultom, H. Abdullah, C.-N. Hsu and D.-H. Kuo, *Chem. Eng. J.*, 2021, **419**, 129608.
35 S. Gupta, M. K. Patel, A. Miotello and N. Patel, *Adv. Funct. Mater.*, 2020, **30**, 1906481.
36 R. Subbaraman, D. Tripkovic, D. Strmcnik, K.-C. Chang, M. Uchimura, A. P. Paulikas, V. Stamenkovic and N. M. Markovic, *Science*, 2011, **334**, 1256–1260.
37 R. Subbaraman, D. Tripkovic, K.-C. Chang, D. Strmcnik, A. P. Paulikas, P. Hirunsit, M. Chan, J. Greeley, V. Stamenkovic and N. M. Markovic, *Nat. Mater.*, 2012, **11**, 550–557.
38 M. G. Siebecker and D. L. Sparks, *J. Phys. Chem. A*, 2017, **121**, 6992–6999.
39 Y. Wang, W. Zhou, R. Jia, Y. Yu and B. Zhang, *Angew. Chem., Int. Ed.*, 2020, **59**, 5350–5354.
40 P. A. Sermon and G. C. Bond, *Catal. Rev.*, 1974, **8**, 211–239.
41 Y. Gorbanev, D. O'Connel and V. Chechik, *Chem. – Eur. J.*, 2016, **22**, 3496–3505.
42 R. Y. Hodgetts, A. S. Kiryutin, P. Nichols, H.-L. Du, J. M. Bakker, D. R. Macfarlane and A. N. Simonov, *ACS Energy Lett.*, 2020, **5**, 736–741.
43 F. Du, J. Li, C. Wang, J. Yao, Z. Tan, Z. Yao, C. Li and C. Guo, *Chem. Eng. J.*, 2022, **434**, 134641.
44 G.-F. Chen, Y. Yuan, H. Jiang, S.-Y. Ren, L.-X. Ding, L. Ma, T. Wu, J. Lu and H. Wang, *Nat. Energy*, 2020, **5**, 605–613.
45 R. Jia, Y. Wang, C. Wang, Y. Ling, Y. Yu and B. Zhang, *ACS Catal.*, 2020, **10**, 3533–3540.
46 C. Wang, Z. Liu, T. Hu, J. Li, L. Dong, F. Du, C. Li and C. Guo, *ChemSusChem*, 2021, **14**, 1825–1829.
47 W. Fu, Z. Hu, Y. Zheng, P. Su, Q. Zhang, Y. Jiao and M. Zhou, *Chem. Eng. J.*, 2022, **433**, 133680.
48 J. Qin, K. Wu, L. Chen, X. Wang, Q. Zhao, B. Liu and Z. Ye, *J. Mater. Chem. A*, 2022, **10**, 3963–3969.
49 A. Aminot, D. S. Kirkwood and R. Kérouel, *Mar. Chem.*, 1997, **56**, 59–75.
50 L. C. Green, D. A. Wagner, J. Glogowski, P. L. Skipper, J. S. Wishnok and S. Tannenbaum, *Anal. Biochem.*, 1982, **126**, 131–138.
51 Y. Xu, K. Ren, T. Ren, M. Wang, M. Liu, Z. Wang, X. Li, L. Wang and H. Wang, *Chem. Commun.*, 2021, **57**, 7525–7528.
52 L. Li, J. Yang, Y. Yun, S. Hu and Y. Huang, *Nanomaterials*, 2020, **10**, 1926.
53 Z. Deng, J. Liang, Q. Liu, C. Ma, L. Xie, L. Yue, Y. Ren, T. Li, Y. Luo, N. Li, B. Tang, A. A. Alshehri, I. Shakir, P. O. Agboola, S. Yan, B. Zheng, J. Du, Q. Kong and X. Sun, *Chem. Eng. J.*, 2022, **435**, 135104.
54 S. Chatterjee, R. K. Parsapur and K.-W. Huang, *ACS Energy Lett.*, 2021, **6**, 4390–4394.
55 I. Chorkendorff and J. W. Niemantsverdriet, *Concepts of Modern Catalysis and Kinetics*, John Wiley & Sons, 2017.
56 H. Prats and K. Chan, *Phys. Chem. Chem. Phys.*, 2021, **23**, 27150–27158.
57 F. Bao, E. Kemppainen, I. Dorbandt, R. Bors, F. Xi, R. Schlatmann, R. van de Krol and S. Calnan, *ChemElectroChem*, 2021, **8**, 195–208.
58 B. K. Simpson and D. C. Johnson, *Electroanalysis*, 2004, **16**, 532–538.
59 O. Q. Carvalho, R. Marks, H. K. K. Nguyen, M. E. Vitale-Sullivan, S. C. Martinez, L. Árnadóttir and K. A. Stoerzinger, *J. Am. Chem. Soc.*, 2022, **144**, 14809–14818.

